ANNALI DI GEOFISICA, VOL. XXXVII, N. 6, December 1994

A study of rupture characteristics of the 40 s subevent of the 1980 Irpinia earthquake

Andres Mendez and Francesca Pacor
ISMES S.p.A., Bergamo, Italy

Abstract
The Irpinia project, as carried out by ISMES under a commission from ENEL, had as objectives the development of a general methodology to simulate broad-band seismic ground motion at near-source and regional distances, and the application of this methodology to the 1980 Irpinia earthquake. Within this general framework, one goal was the comparison of four previously published models for this earthquake in order to arrive at a plausible description of the source process. The comparative study was cast as an inverse problem: that of inferring the spatial extent and temporal behaviour of the rupture process, from geodetic measurements of surface deformation and near-source recordings of ground velocity. This study was complicated by the fact that the Irpinia earthquake was a complex event, involving at least three distinct rupture episodes in a time span of approximately 40 s. However, this same complexity offers the opportunity of illustrating the use of inversion methodologies to: 1) infer the spatial slip distribution on a multiple fault system; 2) address the problem of determining the accuracy of the inferred slip models, and 3) use information describing the static characteristics of an earthquake as an aid in understanding the kinematics of the rupture. This last point is illustrated for the 40 s subevent through the results of a forward modeling study of high-frequency acceleration waveforms using a rupture model based on the inversion results.

Key words *extended source process – inversion – isochron – envelope – strong ground motion*

1. Introduction

The purpose of this paper is to illustrate the use of inversion methodologies to infer earthquake rupture characteristics along faults of finite dimensions. These rupture characteristics include the rupture velocity, the geometry of the rupture front, the spatial distribution of slip and the manner in which the final slip values on the fault are attained. On the one hand, these characteristics are of interest because of the information they provide on the earthquake source process. On the other hand, and especially in the case of complex earthquakes involving the rupture of several faults, it is of interest to see what the inferred rupture characteristics on one fault tell us about the subsequent ruptures on nearby faults. These ideas are illustrated with examples taken from an analysis of the rupture characteristics of the 1980 Irpinia earthquake. This earthquake certainly qualifies as a complex event, as it involved at least three distinct rupture episodes in a time span of approximately 40 s.

Some of the examples presented here form part of a larger project carried out by ISMES under commission from ENEL. The goal of this project was the development of a methodology to simulate near-source and regional ground motion, in terms of acceleration time

histories and site dependent response spectra, taking into account as accurately as possible source, propagation, and site effects. This methodology was then applied to the 1980 Irpinia earthquake, and the problem of determining a plausible source description was approached by comparing four previously published models of this earthquake. The models selected for the comparative study were those of: Westaway and Jackson (1987), Bernard and Zollo (1989), Valensise *et al.* (1989), and a revised version of the model of Fregonese *et al.* (1986). These four models represent a cross-section of more than 80 studies on the source process of the Irpinia event (Valensise, 1993). More recent studies representative of current points of consensus and of discussion regarding the Irpinia source process are those of: Amato and Selvaggi (1993), Bernard *et al.* (1993), Cocco and Pacor (1993), Giardini (1993), Pantosti and Valensise (1993), Pingue *et al.* (1993), Westaway (1993), Sirovich and Chiaruttini (1993), and Vaccari *et al.* (1993).

The comparative study of the four selected models of the Irpinia earthquake was cast as an inverse problem: that of inferring the spatial extent and temporal behaviour of the rupture process, from geodetic measurements of surface deformation and near-source recordings of ground velocity. This paper, however, will concentrate on some of the results obtained for a subevent which initiated 40 s after the main event. Our interest in the 40 s event is twofold: first, it has been one of the least studied events in the Irpinia rupture sequence; and second, its analysis serves the purpose of illustrating the various ideas put forth at the beginning of this paper. The study of the 40 s event is approached from a broad perspective in the first part of this paper, which deals with the inversion of geodetic data to infer the spatial slip distribution on a multiple fault system. The technique is illustrated for two of the four Irpinia fault models previously cited. The subsequent discussion of the different inferred slip distributions will focus on a stability analysis whose goal is to gauge the reliability of their principal characteristics. The second part of the paper deals specifically with the rupture characteristics of the 40 s event. Although this analysis is not based on an inversion methodology, the employed techniques use as input the results of the latter. In particular, we discuss a scenario for the triggering of the 40 s event due to the inferred slip on the main and 20 s event faults and perform a forward modeling of high-frequency acceleration waveforms based on this scenario.

2. Rupture models of the Irpinia earthquake

We consider here only two of the four models included in the comparative study: that of Bernard and Zollo (1989) and that of Valensise *et al.* (1989). As previously mentioned, it is generally agreed upon that the Irpinia rupture sequence involved at least three events. The main event was followed by a rupture episode approximately 20 s after, and one approximately 40 s after initiation of the earthquake. In the Bernard and Zollo model, each episode is associated with a different fault. These faults are depicted in a surface view in fig. 1a where the solid traces represent the vertical projection of the most superficial edge of the faults. The main event fault plane is 30 km in length, dips toward the NE at an angle of 60 degrees, and is buried between 2.2 and 15.2 km in depth. The 20 s event fault plane has a very shallow dip angle and is buried between 10.0 and 15.1 km in depth. The 40 s event fault plane is antithetic to the main event fault plane, dipping toward the SW at an angle of 70 degrees, and measures 20 km in length and 10 km in width.

In the Valensise *et al.* model, the three rupture episodes are proposed to have occurred on a system of 4 faults (fig. 1b). In this case, the main event rupture is divided between two faults separated by the Sele Valley: the M. Marzano - M. Carpineta fault and the Cervialto fault. Although the combined length of these faults (28 km) is similar to the length of the main event fault plane of Bernard and Zollo, the system is translated toward the SE with respect to this latter model. Another major difference with respect to the Bernard and Zollo model is the location of the 20 s event,

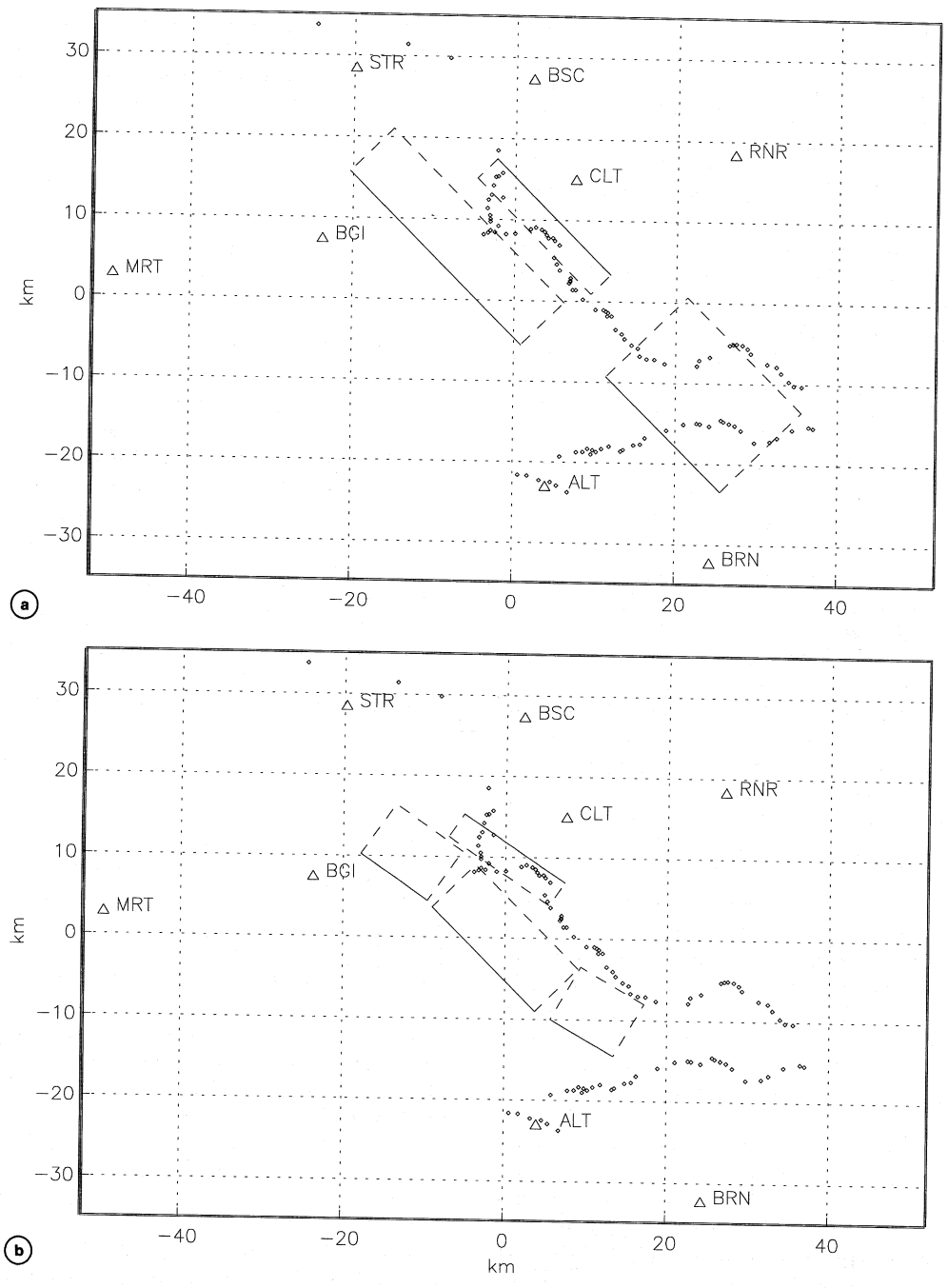

Fig. 1a,b. a) Surface view of the Bernard and Zollo fault model geometry, geodetic benchmarks belonging to the Montocchio-Grottaminarda and Galdo-Tora leveling lines (solid circles), and location of eight ENEL strong motion sites (triangles); b) same as (a) but for the Valensise *et al.* fault model geometry.

situated along the S. Gregorio fault. Finally, the 40 s event fault plane is again placed antithetic to the main event fault plane as originally proposed by Bernard and Zollo, but is of slightly reduced length (15 km).

In addition to the various faults comprising each model, fig. 1a,b displays 8 of the ENEL strong motion sites (triangles) that recorded the earthquake (Berardi *et al.*, 1981), and the geodetic benchmarks (solid circles) belonging to two leveling lines surveyed by the Italian Military Geographic Institute. The Montocchio-Grottaminarda line runs from the SE to the NW. The maximum subsidence recorded along this line was in the order of 75 cm, in the area between the main event and 40 s event fault planes. The Galdo-Tora line is located towards the south of these faults and experienced a maximum subsidence of approximately 10 cm.

The value of the geodetic data set has been cast into doubt by the fact that the leveling campaigns were performed only twice over a time interval of 22 years. It is therefore quite reasonable to question whether the observed height differences can be attributed solely to the Irpinia earthquake. Cotecchia *et al.* (1990) have presented arguments to the effect that the height differences are to a large extent an expression of the earthquake. The essence of these arguments is that the measured subsidence along portions of the Montocchio-Grottaminarda line is comparable to the measured subsidence along secondary lines which were surveyed in different overlapping time frames which include the time of the Irpinia earthquake. Although one cannot conclude that the surface deformation in the area of Irpinia was due solely to the earthquake, this evidence indicates that a predominant part was of coseismic nature.

The degree of predominance of coseismic deformation over other processes is, however, difficult to assess. This uncertainty in the geodetic data will also produce uncertainty in the inferred features of the slip model obtained from the inversion process. It is possible to address this problem by performing the inversion not only for the best fault slip model, but also for a family of slip models which are compatible with the data in the sense of misfitting it within a permitted tolerance. This inversion methodology and subsequent analysis to determine the reliability of the inferred slip distributions are briefly described in the following section.

3. Inversion methodology

3.1. *Formulation of the inverse problem for coseismic slip*

The employed inverse methodology is based on the forward model of an earthquake as a spatial and time dependent slip discontinuity across the surface of one or more rectangular fault planes. The elastodynamic representation theorem, as expressed in the frequency domain, is used to linearly relate slip velocity on the fault with ground velocity (Spudich, 1980; Olson and Anderson, 1988). At 0 Hz, this linear relation reduces to one between coseismic slip and surface deformation and can be represented by the following matrix equation:

$$\boldsymbol{G}\boldsymbol{s} = \boldsymbol{d} \tag{3.1}$$

In eq. (3.1) the unknown quantity, $\boldsymbol{s}$, represents the spatial varying slip on the fault in terms of its values at N subfaults into which the fault (or faults) of interest are subdivided. The matrix $\boldsymbol{G}$ is comprised of Green's function for each subfault and relates the slip on the subfault with the recorded surface data. These latter are grouped into the vector $\boldsymbol{d}$. It is important to note that eq. (3.1) contains several implicit assumptions. For one, it is assumed that the geometry of the fault plane is known. The second assumption is that slip on the fault is parallel to its surface and, although a spatial variability in amplitude is permitted, the rake of the slip vector remains constant.

It is possible to introduce further physical assumptions regarding general characteristics of the unknown slip distribution by appending additional equations to the original system (3.1). These assumptions usually regard con-

straints on the degree of permissible roughness of the solution (Olson and Apsel, 1982; Hartzell and Heaton, 1983; Hartzell, 1989, for example) and can also take the form of boundary conditions that the solution should satisfy at the fault edges (Cohee and Beroza, this volume, page 1515, for example). Another approach consists in modifying the matrix $\boldsymbol{G}$ in such a way that the fundamental physics of the problem, given by the elastodynamic representation theorem, remains fulfilled. One such approach is described in Mendez *et al.* (1990) when performing the inversion for slip velocity in the frequency domain. At 0 Hz, this approach is equivalent to that of Harris and Segall (1987). For the purpose of illustrating this method, let $\boldsymbol{D}$ be the matrix representation of the Laplacian operator. The original linear system (3.1) can be transformed by inserting the identity matrix in the form $(\boldsymbol{D}^{-1}\boldsymbol{D})$, and solving for the new unknown $\boldsymbol{u} = (\boldsymbol{D}\boldsymbol{s})$:

$$\boldsymbol{G}\,(\boldsymbol{D}^{-1}\boldsymbol{D})\,\boldsymbol{s} = \boldsymbol{d} \qquad (3.2a)$$

$$(\boldsymbol{G}\boldsymbol{D}^{-1})\,\boldsymbol{u} = \boldsymbol{d} \qquad (3.2b)$$

after which the spatial slip distribution is recovered from:

$$\boldsymbol{s} = (\boldsymbol{D}^{-1}\boldsymbol{u})\,. \qquad (3.2c)$$

The reason for the transformations embodied in eqs. (3.2a) and (3.2c) is to take advantage of the fact that there is a unique solution to the linear system with minimal 2-norm. If $\boldsymbol{u}$ is the minimal 2-norm solution of eq. (3.2b), then $(\boldsymbol{D}\,\boldsymbol{s})$ also has a minimum 2-norm. Since $\boldsymbol{D}$ represents the Laplacian operator, which involves spatial derivatives, the fact that the 2-norm of $(\boldsymbol{D}\,\boldsymbol{s})$ is minimal is equivalent to stating that the linear system (3.2b) and (3.2c) has been solved for the smoothest spatial slip distribution $\boldsymbol{s}$ which best fits the data. Thus the resulting solution for the slip distribution is devoid of spurious features that are permitted but not actually required by the data, and retains only those features that can be resolved to within the limits imposed by the layout (or geometry) of the surface observations (Olson and Anderson, 1988; Mendez *et al.*, 1990).

3.2. *Stability analysis*

The goal of the stability analysis is to provide a quantitative estimate of the influence that possible errors in the geodetic data set can have on the slip model obtained through the inversion process. The approach used here is that originally developed in Olson and Apsel (1982). The solution to eqs. (3.2b) and (3.2c) will yield a slip model $\boldsymbol{s}$ which produces a least squares fit to the geodetic data $\boldsymbol{d}$ with a misfit determined by the number of singular values of $(\boldsymbol{G}\,\boldsymbol{D}^{-1})$ that are retained. We will refer to this least squares slip model as $\boldsymbol{s}_{ls}$. If the geodetic measurements were free of error and if the forward model relating slip on the fault to surface deformation was perfectly accurate, $\boldsymbol{s}_{ls}$ would qualify as the best slip model among all others producing larger misfits. However, since both the data and forward model are likely to contain errors, any slip model producing a slightly larger misfit could also be accepted as reasonable. The stability analysis seeks to identify a particular subset of these other acceptable slip models, as described in the following. It is carried out by first defining a tolerable amount of misfit; and then finding the largest possible variation that each component (each slip value) of $\boldsymbol{s}_{ls}$ can undergo without degrading the initial least squares fit by more than the stated tolerance. This analysis produces a family of slip models, where one component (one slip value) of each of the models deviates in this extremal sense from its corresponding component in $\boldsymbol{s}_{ls}$.

In order to quantify the above discussion, let δs_j represent the just defined maximum variation that the jth component of $\boldsymbol{s}_{ls}$ can undergo. The relation between the slip model presenting this maximum variation and the least squares slip model $\boldsymbol{s}_{ls}$ is:

$$\boldsymbol{w}_j^T\,\boldsymbol{s} = \boldsymbol{w}_j^T\,\boldsymbol{s}_{ls} + \delta s_j \qquad (3.3)$$

where $\boldsymbol{w}_j$ is a vector with all components equal to zero except for the jth component, which is set to one. The superscript T in eq. (3.3) denotes the transpose of a vector. Next, let $\Delta\boldsymbol{d}$ represent the residual vector between the data vector produced by $\boldsymbol{s}_{ls}$ and the data vector produced by any of the extremal slip models de-

fined in eq. (3.3). The prescribed tolerance, δd, is then defined as:

$$\delta d = (\Delta \boldsymbol{d}^T \Delta \boldsymbol{d})^{1/2} \qquad (3.4)$$

Following Olson and Apsel (1982), it can be shown that the relation between δs_j and δd for the inverse problem embodied in eqs. (3.2a) through (3.2c) is:

$$\delta s_j = \pm\ (\boldsymbol{w}_j^T \boldsymbol{D}^{-1} \boldsymbol{V} \Lambda^{-2} \boldsymbol{V}^T \boldsymbol{D}^{-1} \boldsymbol{w}_j)^{1/2}\ \delta d \qquad (3.5)$$

where the matrix Λ contains the singular values, and the matrix $\boldsymbol{V}$ the right singular vectors, that are retained in the singular value decomposition of the matrix $(\boldsymbol{G}\boldsymbol{D}^{-1})$ of eq. (3.2b). In practice, for the case of a fault discretized by subdivision into N subfaults, each one of the N extremal variations or bounds, δs_j, is obtained by solving eq. (3.5) using the corresponding weight vector $\boldsymbol{w}_j$. The final result of this type of stability analysis consists in a family of slip models which misfit the true data within a fixed tolerable amount. The seismic moment of any of these slip models can be obliged to fall within certain limits by a simple scaling procedure. Instead of presenting each possible slip model with its corresponding data fit, the results are summarized graphically in the following manner:

a) the least squares data fit is displayed together with «error» bars. These error bars define the band of acceptable data fits. The size of the error bars is related to the predefined tolerance δd, a larger tolerance results in a wider band. The value of the tolerance is selected so that the band of acceptable data fits encompasses the true data vector as far as possible;

b) the least squares slip model is sandwiched between two extremal slip models. These two extremal models represent bounds on the maximum possible variations in the values of slip on the fault. The most important point to note is that any slip model outside of these bounds will necessarily produce a data fit outside of the band of acceptable data fits described above in (a).

4. Application to the Irpinia earthquake

In the context of the Irpinia earthquake, the idea behind the comparative study was to identify recurrent features of the inferred slip models obtained using the different proposed fault geometries. These common features could then be attributed a physical significance, especially if they continued to appear in the stability analysis.

It should be noted that the two fault models briefly outlined in section 2 differ not only in their geometries, but also in the amount of slip that the two groups of authors propose to have occurred on the various faults of their models. This information was incorporated into the inversion by forming a new data vector:

$$\boldsymbol{d}' = \boldsymbol{d} - (\boldsymbol{G}\,\boldsymbol{s}_0) \qquad (4.1)$$

where $(\boldsymbol{G}\,\boldsymbol{s}_0)$ denotes the resulting fit to the geodetic data from the proposed constant slip models. The inversion was then performed using this new data vector $\boldsymbol{d}'$ in place of the original $\boldsymbol{d}$ in eqs. (3.2a) and (3.2b). The inferred slip distribution $\boldsymbol{s}$ was then added to the initial constant slip distribution $\boldsymbol{s}_0$ to obtain the final slip model.

Figure 2 is a partial summary of the results of inverting the geodetic data using the fault system proposed by Valensise *et al.* (on the left hand side) and that of Bernard and Zollo (on the right hand side). It is a partial summary as it only displays the data fit to the Montocchio-Grottaminarda line, although the data from the two lines were jointly inverted. In this figure, the solid trace represents the data while the dashed line is the fit obtained from the inversion. The dotted line represents the contribution to the overall fit from the inferred slip on each fault. In other words, summing the dotted line values along a column yields the dashed line values.

A first observation that can be made regarding these results is that slip on the main event and 40 s event fault planes dominates the fit to the Montocchio-Grottaminarda line. Slip on the 20 s event fault plane has only a slight influence in determining vertical deformation along this line. The second observation is that the

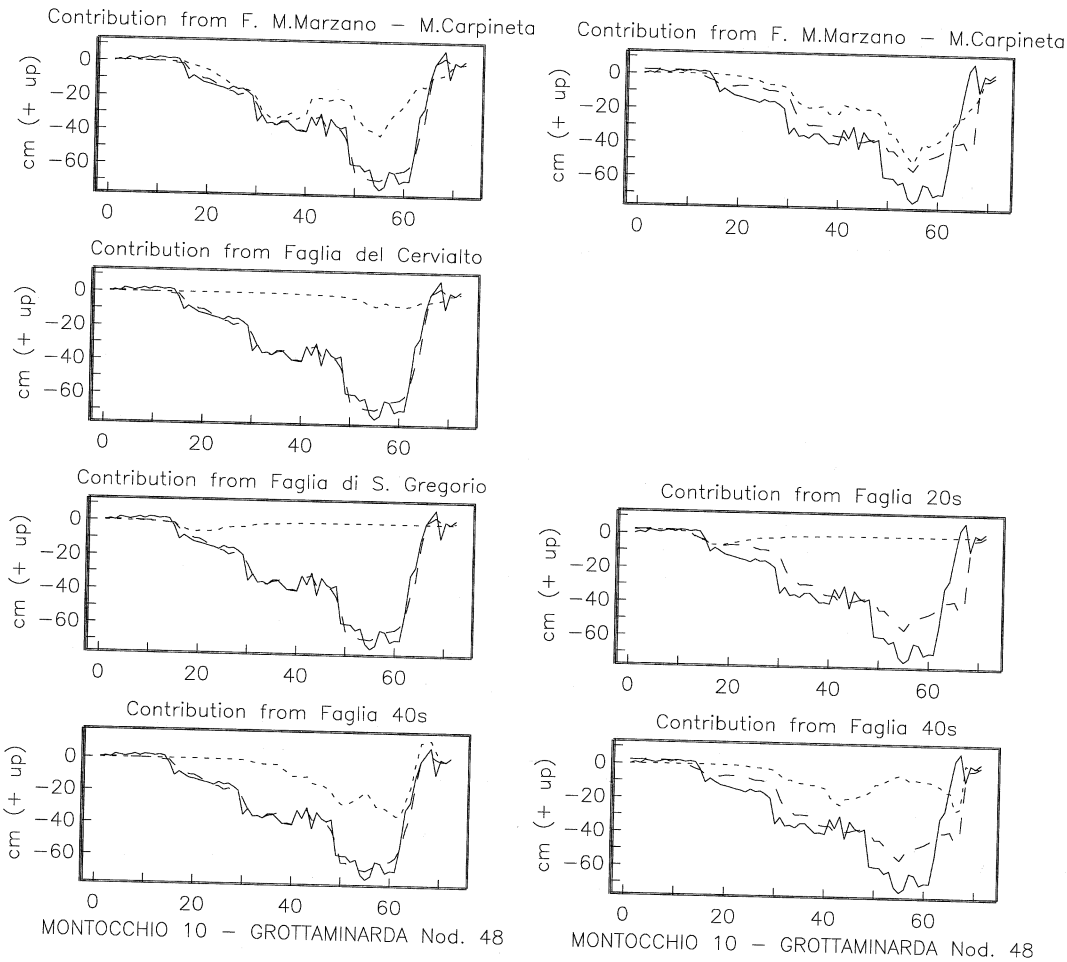

Fig. 2. Contributions to the data fit to the Montocchio-Grottaminarda leveling line from the individual faults comprising the Valensise *et al.* model (first column), and Bernard and Zollo model (second column). The solid trace is the data and the dashed trace is the best fit from the inversion. The best fit is decomposed into contributions (dotted traces) from slip on the individual faults.

placement of the 40 s event fault plane appears critical in determining the quality of the overall fit to Montocchio-Grottaminarda. While in both models slip on the main event fault plane produces a fit which displays the same trend as the data, slip on the 40 s event fault plane is very important in modeling the sharp gradient observed in the NW portion of the line (data points numbered from 60-70, approximately). In fact, by replacing the 40 s event fault plane of the Bernard and Zollo model with that of the Valensise *et al.* model and repeating the inversion, the data fit improves greatly to the point of becoming almost indistinguishable from the fit obtained using the Valensise *et al.* fault system.

Figure 3 compares the inferred spatial slip distributions when the inversion is performed using the Valensise *et al.* fault system and when performed using this hybrid model which

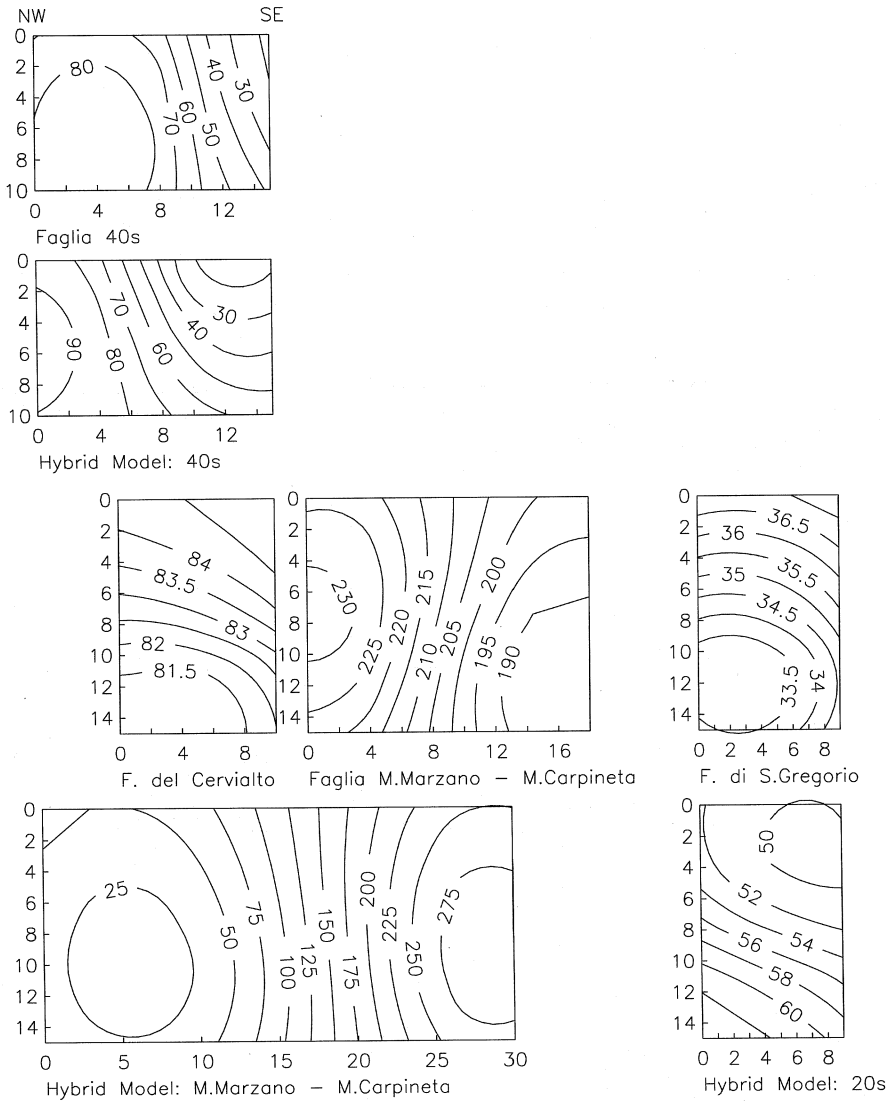

Fig. 3. Comparison of inferred slip distributions when inverting the geodetic data using the Valensise *et al.* fault system (bottom illustrations), and when using a hybrid model combining the main event fault of Bernard and Zollo with the Valensise *et al.* faults for the 20 s and 40 s events (top illustrations). Contours represent pure dip-slip amplitudes in units of cm.

combines the main event fault of Bernard and Zollo with the Valensise *et al.* faults for the 20 s and 40 s events. In this figure, the relative displacement between the main event fault plane of the two models is intended to represent the NW translation of the Bernard and Zollo fault some 5 km with respect to the main event (M. Marzano-M. Carpineta and Cervialto) fault planes in the Valensise *et al.* model.

It is seen that the spatial slip distributions on the 40 s event fault plane in both models are very similar; the largest slip amplitudes are located in the NW portion, and tend to decrease rapidly toward the SE. Of course, the 40 s event fault plane in these two models is identical in geometry. So one can expect that these two slip distributions contribute to the fit to Montocchio-Grottaminarda in a similar fashion. The remaining fit has to be made up predominantly from slip on the main event. In this case, the difference in fault geometries produces what at first appears as considerably different slip distributions. The trend in the spatial slip distribution on the Bernard and Zollo main event fault is to decrease going from the SE to the NW. A similar trend is present in the Valensise *et al.* model as one jumps from one fault to the other, but on the M.Marzano-M. Carpineta fault the slip decreases in value as one goes from the NW to the SE.

The stability analysis described in section 3.2. is useful in determining if the above features of the inferred slip distributions are actually necessary to fit the data. This is illustrated for the case of the Valensise *et al.* model in figs. 4 and 5. The solid trace in fig. 4 again represents the vertical surface deformation as measured along the Montocchio-Grottaminarda line. The dotted trace represents the fit assuming the original spatially constant slip distribution proposed in this model. The dashed trace is the fit from the inversion process. This least squares fit is now enveloped in a band formed by the vertical bars. This band is obtained from the stability analysis and represents the family of acceptable data fits. Although the band of acceptable data fits overlaps the original data fairly well, it should be noted that the overlap with the constant slip model is generally poorer. This would imply the need for a spatially varying slip distribution to model the data correctly.

Figure 5 displays the two extremal slip models obtained from the stability analysis. We recall that this analysis insures that any slip distribution with values outside of these extremal models will necessarily produce a

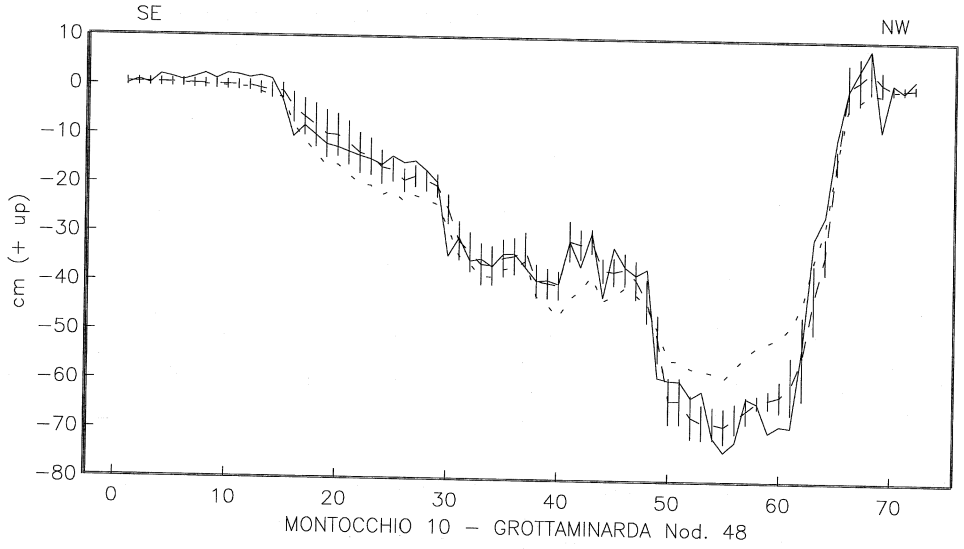

Fig. 4. Summary of the stability analysis applied to the Valensise *et al.* model. The solid trace is the vertical surface deformation measured along the Montocchio-Grottaminarda benchmarks. The dotted trace represents the fit assuming a constant slip distribution on each of the faults comprising this model. The dashed trace is the fit from the inversion. The band of acceptable data fits is represented by the vertical bars.

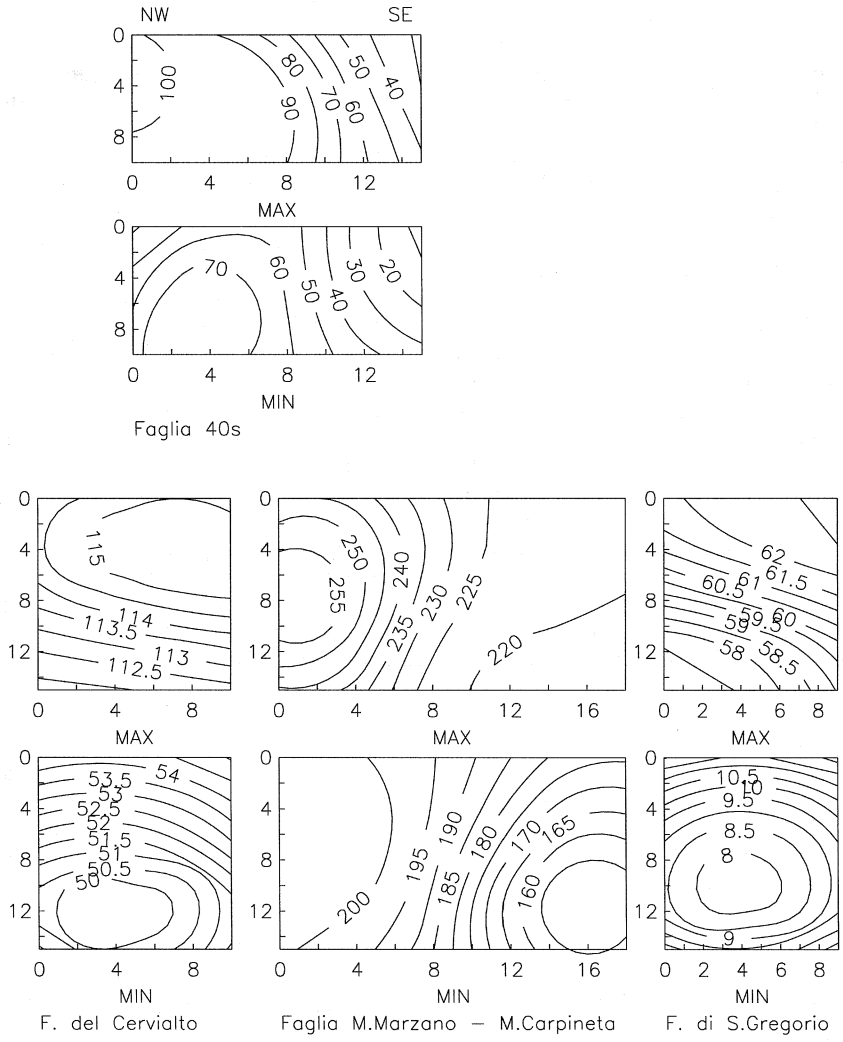

Fig. 5. Summary of the stability analysis applied to the Valensise *et al.* model. The two slip models represent the upper and lower bounds on variations in the spatial slip distribution. Any slip model with amplitudes outside these bounds will produce a data fit outside of the band of acceptable data fits shown in fig. 4. Contours are in units of cm. Horizontal scale exaggerated by a factor of 1.5.

data fit outside the band of acceptable data fits shown in fig. 4. As stated previously, an analysis of this sort provides additional information on the inferred slip distributions. For example, in the case of the 40 s event fault plane, the maximum and minimum slip envelopes both exhibit the same strong trend for slip to decrease from the NW to the SE. The minimum slip value on the maximum envelope is always less than the maximum slip value on the minimum envelope. This is then a strong indication that the area of large slip amplitudes is actually real.

Similarly, the envelopes for the main event

Table I. Summary of geodetic inversion: Valensise *et al.* fault model.

Fault ID	S_0 (cm)	S_f (cm)	M_0 (10^{18} Nm)	M_0 (S_f) (10^{18} Nm)	Max M_0 (10^{18} Nm)	Min M_0 (10^{18} Nm)
# 1 M. Marzano-M. Carpineta	200.	208.	16.2	16.8	18.3	15.4
# 2 Cervialto	100.	83.	4.5	3.7	5.1	2.3
# 3 S. Gregorio	70.	35.	2.8	1.4	2.4	0.4
# 4 '40 s'	50.	61.	2.3	2.8	3.1	2.5
All	–	–	25.8	24.7	26.1	23.5

also point to a decrease in slip values as one jumps from the M.Marzano-M.Carpineta fault to the Cervialto fault. Slip values on the maximum envelope of the Cervialto fault never exceed slip values on the minimum envelope of the M. Marzano-M. Carpineta fault. But on analyzing only the slip envelopes for the M.Marzano-M.Carpineta fault, it is difficult to judge whether the trend for slip to decrease in value from the NW to the SE is strictly required to fit the geodetic data. The extremal models simply are not tight enough to exclude the possibility of models with the opposite trend in slip amplitudes.

We conclude this section by summarizing the results of the inversion and stability analysis for the model of Valensise *et al.* in table I. In this table, s_0 is the constant value of slip proposed in this model for each fault, while s_f is the average slip found from the inversion. Columns 4 and 5 are estimates of seismic moment assuming a constant shear modulus of 3×10^{10} N/m^2. Column 4 corresponds to the initial constant slip model while column 5 refers to the value obtained using the slip model obtained from the inversion. The total seismic moment is tabulated along the row with fault ID «All», and is simply a scalar sum of individual fault moments. The last two columns contain the seismic moments associated with the family of slip models obtained from the stability analysis. It should be noted that the sum of minimum moments for individual faults does not add up to the minimum total moment. The same observation applies for the maximum moment. This reflects the fact that the two extremal models which contain the family of acceptable slip models do not themselves produce data fits which lie in the band of acceptable data fits. The two extremal models are not to be thought of as acceptable models but rather as bounds on the maximum possible variations in slip which the best model can exhibit, while still fitting the data to within some acceptable tolerance.

5. Initiation of the 40 s event rupture

The lack of an absolute time scale for the strong motion recordings of the Irpinia earthquake has been a major obstacle in their study. The different models for this earthquake all propose different hypocenters for the various subevents. In part, this is due to the impossibility of specifying one unique timing scenario without more stringent constraints coming from the data.

In this section, we explore the possibility of using the results of the geodetic inversion as an

aid in determining a plausible hypocenter for the 40 s event. The analysis is based on the rather sharp drop in slip values which occurs between the M.Marzano-M.Carpineta fault and the Cervialto fault, as inferred from the inversion. The area between these two faults is occupied by the Sele Valley, and Pantosti and Valensise (1990) identified surface faulting on either side of the valley but not within the valley. The question we have posed is: what does the resulting strain field look like in the vicinity of the 40 s event fault plane, assuming the inferred spatial slip distributions on the main and 20 s event fault planes of the Valensise *et al.* model and assuming that no slip occurred in the Sele Valley? Through the analysis of the strain field, the idea was to identify possible areas where the normal stress across the 40 s event fault plane had diminished, therefore facilitating its rupture. This hypothesis is equivalent to the Coulomb criterion for brittle fracture (see for example, Turcotte and Schubert, 1982).

To be more specific, we calculated the displacement field on two planes parallel to the 40 s event fault, and situated on either side of the fault, using the analytic expressions derived by Okada (1992) for the internal deformation of a halfspace due to shear faults. In this calculation, the average values of slip on the main (M.Marzano-M.Carpineta and Cervialto) and 20 s event fault planes inferred from the geodetic inversion (and reported in table I) were used as opposed to the inferred spatially varying slip distributions. The two planes placed on opposite sides of the 40 s event fault define a thin rectangular volume, a pillbox, and the calculated displacement fields were subtracted and then projected along the vector normal to these planes in order to obtain the net extension across the pillbox. Figure 6 is a contour plot of the resulting net extension across the 40 s event fault plane in units of cm, but the contour values can be interpreted as the component of the strain field normal to the fault plane after scaling by a factor of 10^{-4}.

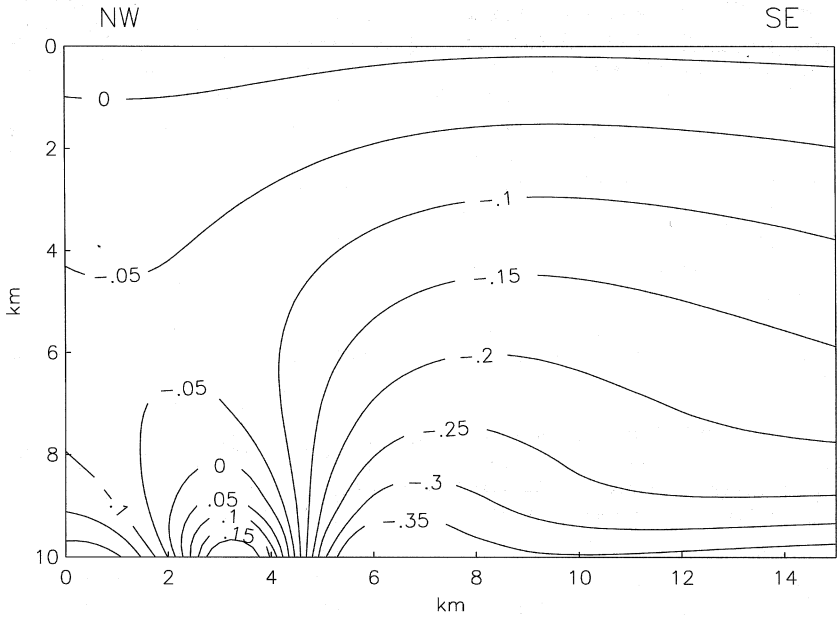

Fig. 6. Planar view of the net extension across a pillbox surrounding the 40 s event fault plane. Contour values are in units of cm, negative values represent a net compression while positive values a net extension.

In fig. 6, the superficial edge of the pillbox volume enclosing the 40 s event fault plane is buried at a depth of 2 km. As one proceeds to greater depths along the dip direction, one can observe that starting at approximately 1-2 km downdip from the top edge, the 40 s event fault plane experiences a net compression (negative contour values) except for a small portion which experiences a net extension (positive contour values). It is interesting to note that this area of net extension on the 40 s event fault plane is located on that part of the fault which crosses the Sele gap between the M. Marzano - M. Carpineta and Cervialto faults (fig. 1b). If the net extension can be translated into a reduction of normal stress across the 40 s event fault plane, then these results suggest this area as a plausible nucleation point for the 40 s event rupture.

A stronger argument for a cause-and-effect relation between the lack of slip in the area of the Sele Valley and the nucleation area of the 40 s event could be made from an analysis of arrival times in the strong motion records. An analysis along these lines was performed by Bernard and Zollo, indicating that the hypocenter of the 40 s event is located in the NW section of the fault. This analysis is not straightforward since the records lack an absolute time scale. This problem also hinders an independent confirmation of the location of the 40 s event hypocenter which could be obtained by inverting the strong motion records for the rupture characteristics of this event. Another difficulty of performing such an inversion is the fact that the ground motion time histories associated with the 40 s event also present energy from the main event. This is especially evident in the integrated acceleration records where low period (< 1 Hz) reverberations precede and then mix with wave arrivals from the 40 s event (fig. 7). At higher frequencies though, the signal from the 40 s event increasingly tends to dominate. This fact suggests the possibility of modeling the high-frequency ground motion from the 40 s event, based on information of the rupture gained from the geodetic inversions. The following section describes the methodology and results of this approach.

6. Forward modeling of high-frequency acceleration records

The modeling of high-frequency acceleration records is based on the calculation of radiated seismic energy using the isochron formulation of Bernard and Madariaga (1984) and Spudich and Frazer (1984). Rather than attempt to model the high-frequency oscillations observed in the ground motion time histories, our efforts were directed towards modeling the envelope of these oscillations. In principle, this latter approach would seem more robust to inaccuracies regarding the description of the small scale features of rupture and medium of propagation.

In our application of the isochron formulation, propagating Dirac delta functions scaled by geometrical spreading were used as Green's functions. Propagation times from each portion of the fault to the site of interest were calculated by raytracing. In addition, a random phase was introduced in the Green's functions. In this manner, the contribution to ground motion at a given site due to each isochron is calculated as an incoherent sum of the emitted radiation. The final step in the calculation of synthetic envelopes consists in smoothing the obtained time histories with a running mean filter.

Since the calculation of synthetic envelopes is based on the use of simplistic Green's functions, the amplitudes of ground motion will in general be different from those calculated using Green's functions representing the exact response of the medium. However, the relative amplitudes of ground motion between one site and another should be similar to those obtained using the exact response of the medium. For the purpose of comparing with the data, all the synthetic envelopes were scaled by the same constant factor.

The synthetic envelopes were calculated for shear wave motion only from a 40 s event rupture scenario with the following characteristics. The rupture nucleates at a point centered in the area which in section 5. was found to have suffered a net extension due to slip on the main and 20 s event fault planes. This point is located 9 km down dip from the most superficial

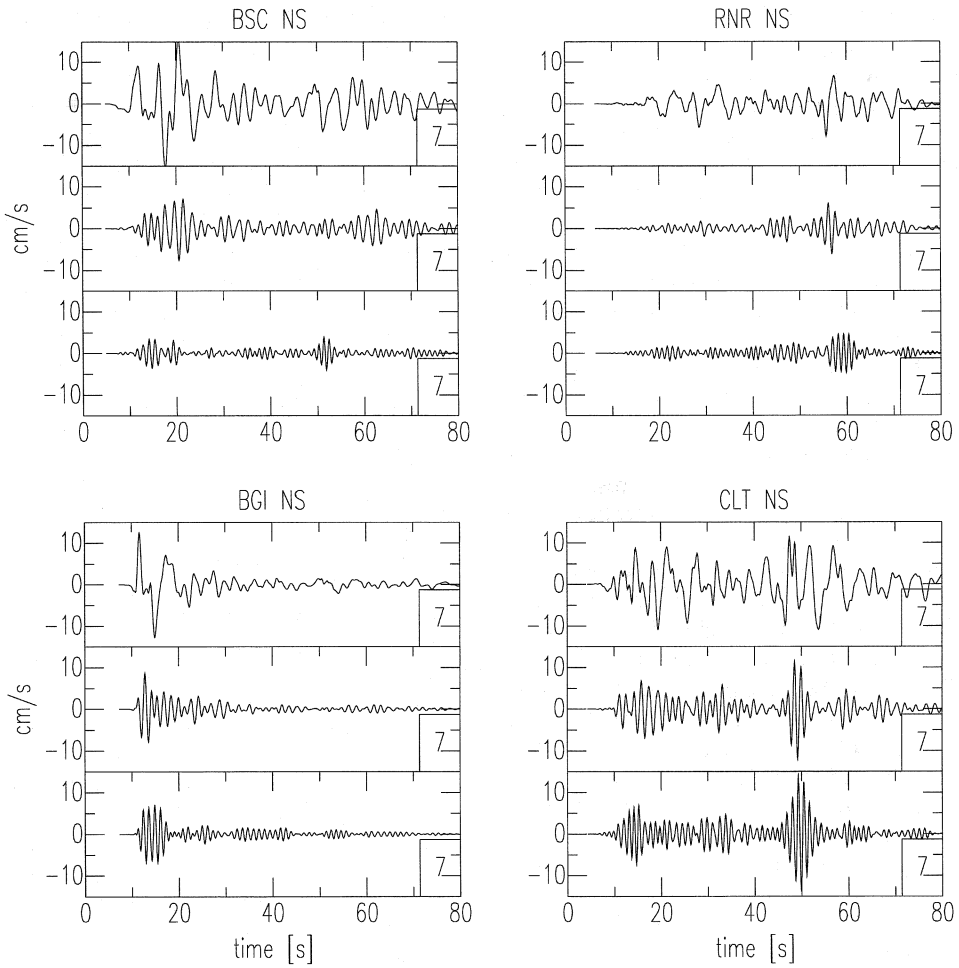

Fig. 7. NS component of velocity time histories, integrated from the corresponding ground accelerations recorded during the Irpinia earthquake at four ENEL strong motion sites: Bisaccia (BSC), Rionero in Vulture (RNR), Bagnoli (BGI) and Calitri (CLT). Time histories are bandpassed filtered between 0.1-0.5 Hz (top trace), 0.5-0.75 Hz (middle trace), and 0.75-1.0 Hz (bottom trace). The time histories have been aligned as proposed by Bernard and Zollo, implying that wave arrivals from the 40 s event cannot come in earlier than at least 40 s into the recordings.

edge of the 40 s event fault plane and 3.5 km from its NW edge. From this point, the rupture propagates radially outward, deviating slightly from a perfectly circular rupture front by the addition of a small stochastic component to the rupture times. Following Spudich and Frazer (1984), the calculation of ground motion is performed by integrating over isochron strips. The rupture velocity was set to a value of 2.2 km/s. The spatial slip distribution on the fault corresponds to that found from the inversion of the geodetic data using the fault geometry proposed by Valensise *et al.* (1989).

The velocity model used for raytracing is a

simplified version of that used by Bernard and Zollo for the Irpinia region and has the following characteristics. The shear wave velocity in the first layer of 3 km thickness is 1.26 km/s. In the second layer, 4 km thick, the shear wave velocity is 2.96 km/s. Finally, the shear wave velocity of the underlying halfspace is 3.46 km/s.

Regarding the data processing, the definition of envelope as the modulus of the analytic signal (Bracewell, 1978) was used in the calculation of the acceleration time history envelopes. Prior to this step, it was necessary to determine the duration of the time histories to be used in the formation of the analytic signal. The criterion that we selected was that of Trifunac and Brady (1975) and is defined as the time interval for the normalized Arias' intensity (1969) to build up from the 5 to 95 percent value. Figures 8a-d illustrate these ideas for the EW component of acceleration at the ENEL sites: Bagnoli (BGI), Auletta (ALT), Bisaccia (BSC), and Brienza (BRN), respectively. For each site, two curves are displayed. The bottom trace is the actual acceleration time history. The top trace is a Husid (1969) plot of normalized Arias' intensity. The normalized Arias' intensity, denoted by $h(t)$, is defined as:

$$h(t) = \frac{\int_0^t a^2(\tau)\, d\tau}{\int_0^T a^2(\tau)\, d\tau} \qquad (6.1)$$

where T is the total duration of the acceleration record, a. The vertical lines in the Husid plot are also present in the acceleration time history and represent the effective duration of ground shaking using the definition of Trifunac and Brady.

Figures 9a-d compare the synthetic envelopes with the acceleration time history envelopes for the ENEL sites BGI, ALT, BSC, and BRN, respectively. Both horizontal components for each site are confronted with the same synthetic envelope. At present we have not introduced the effect of the radiation pattern in the synthetic calculations. The data envelopes are shown with a solid trace, while the synthetic envelope is shown with a dashed trace.

The duration of the synthetic envelopes is very close to that of the data for the sites nearest the fault: BGI and BSC. For both ALT and BRN, the mismatch in duration is always greater than 4 s. A possible explanation for the discrepancy in durations lies in the fact that the synthetic envelopes are calculated based on direct arrivals of shear waves from the extended fault to the sites. The actual data also contain multipath arrivals, such as those from scattered energy. As noted by Dobry *et al.* (1978), different wave arrival regimes can be approximately associated with different slopes in a Husid plot. In the case of ALT, the corresponding Husid plot does exhibit a clear change in slope at approximately 8 s, which would imply that the theoretically calculated duration (6.9 s) is in accord with the duration of direct arrivals for this site (5.9 s). A similar argument could perhaps be used for BRN, but in this case it is difficult to identify a unique time after which the predominant contribution to ground motion is from multipath arrivals.

A comparison between data and synthetics can also be made in terms of amplitudes and waveform shapes. In figs. 9a-d, it is seen that the synthetic amplitudes are in general agreement with the true amplitudes. The greatest discrepancies are observed for ALT (overestimated in the middle part of the traces), and BSC (underestimated in the later part of the traces). Regarding the shape of the synthetic envelopes, the resemblance with the data varies in quality. Laying aside the mismatch in amplitudes, some examples of features which are reproduced in the synthetics are: the waveform shape of the WE component of ALT, at the beginning and end portions of the synthetic envelope, the waveform shape of the NS component of BSC, especially in the first 2 and last 3-4 s; the middle portion of both components at BRN; and finally, the waveform shapes of both components at BGI, especially the NS.

In summary, although this example of forward modeling of acceleration envelopes does not prove the proposed rupture scenario for the

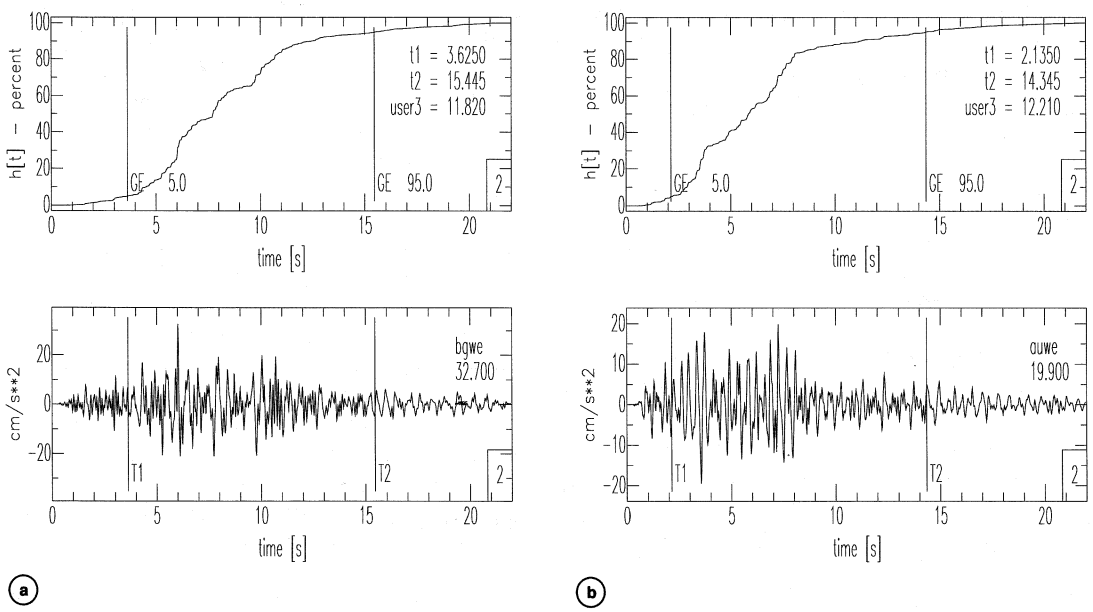

Fig. 8a,b. a) 40 s event acceleration time history (EW component) recorded at BGI (bottom) and Husid plot of normalized Arias' intensity (top); b) same as (a) but for the recording site ALT.

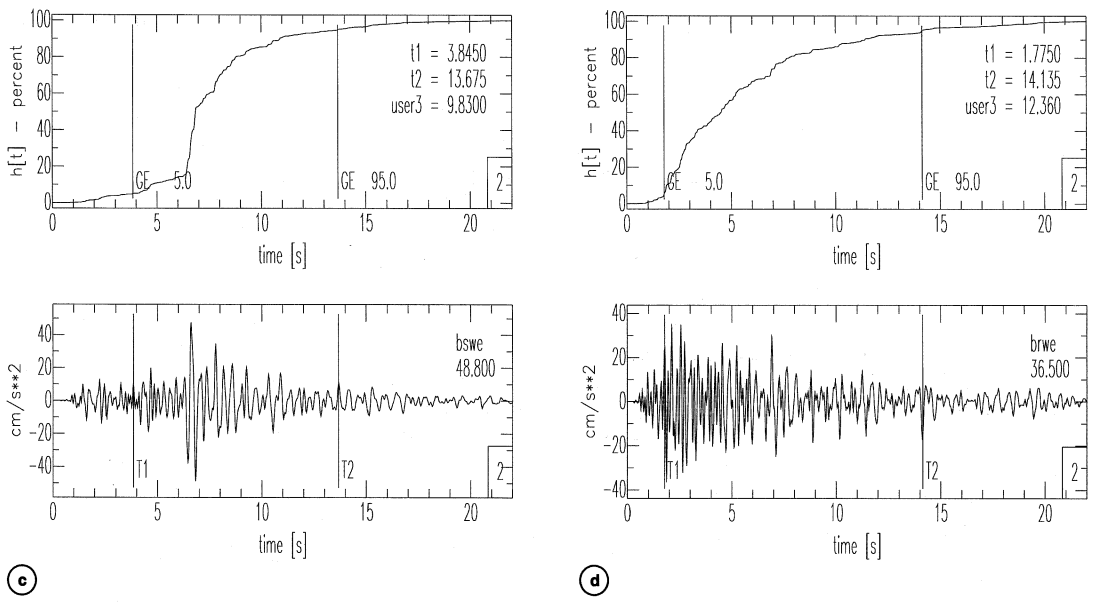

Fig. 8c,d. c) 40 s event acceleration time history (EW component) recorded at BSC (bottom) and Husid plot of normalized Arias' intensity (top); d) same as (c) but for the recording site BRN.

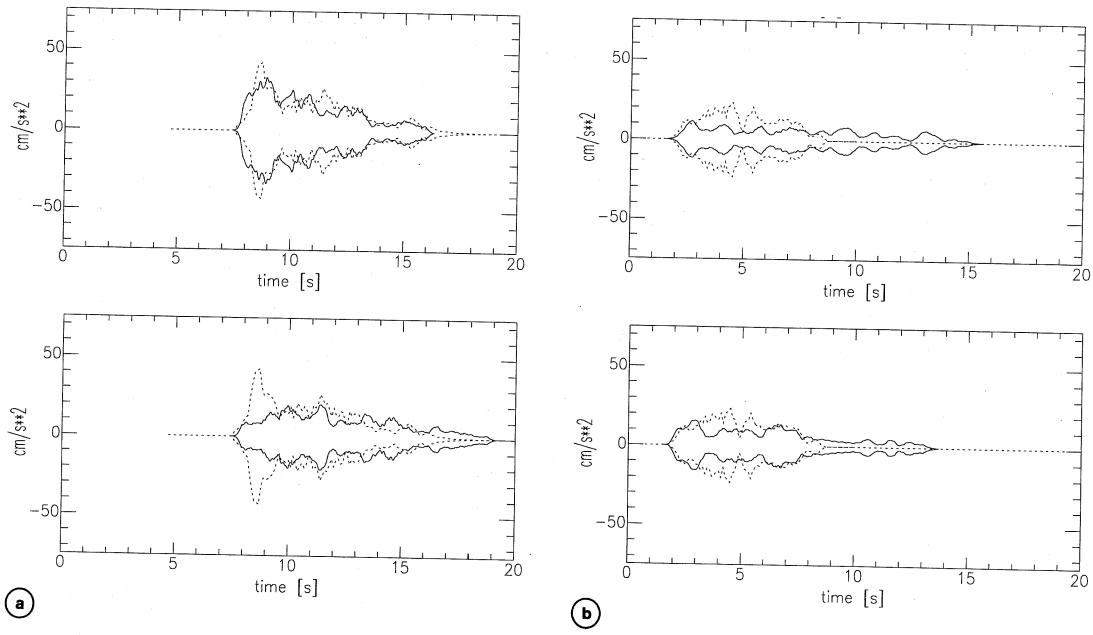

Fig. 9a,b. a) NS (top) and WE (bottom) 40 s event acceleration time history envelopes and synthetic envelope for BGI; b) same as (a) but for the recording site ALT.

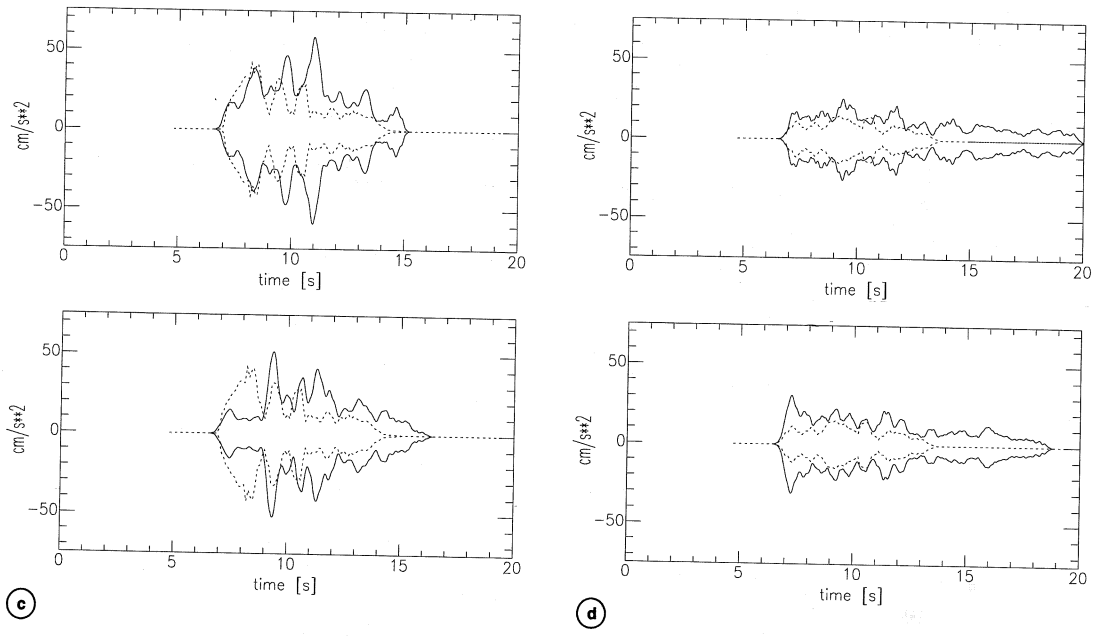

Fig. 9c,d. c) NS (top) and WE (bottom) 40 s event acceleration time history envelopes and synthetic envelope for BSC; d) same as (c) but for the recording site BRN.

40 s event, the results would seem consistent with the scenario constructed from the geodetic inversion study.

7. Conclusions

This paper has dealt with the following issues regarding the use of inversion methodologies in the study of earthquakes: 1) the inversion of geodetic data to infer the spatial slip distribution on a multiple fault system; 2) the problem of assessing the accuracy of slip models inferred from inaccurate data, and 3) the possibility of utilizing information describing the static characteristics of an earthquake as an aid in understanding the kinematics of the rupture. These issues were discussed and illustrated through examples from a comparative study of the 1980 Irpinia earthquake using an inverse theory approach.

The major point to be stressed regarding the geodetic inversion is that the recurrent features of inferred slip distributions are those which can be most safely attributed a physical significance. The stability analysis repeats this point by providing bounds on the possible variations exhibited by slip models which fit the data to within a certain tolerance and whose seismic moment is within certain limits. Examples of the application of this stability analysis technique to time domain inversions can be found in Olson and Apsel (1982), Hartzell and Iida (1990), and Mendez and Luco (1990).

The clear identification of at least three subevents in the Irpinia rupture sequence offers the opportunity of studying the mechanism by which its constituent faults might have interacted. An example was presented in which we calculated the strain field in the vicinity of the 40 s event fault, induced by the inferred slip on the main and 20 s event fault planes. A simple hypothesis based on the reduction of normal stress was put forth as a possible indicator of the location of the nucleation point of the 40 s event. This analysis was completely static; the problem of studying the influence of dynamic stresses created by the rupture of the main and 20 s event faults was not addressed. The general problem of seismicity induced by an earthquake is discussed in further detail and also at different time and length scales in papers by Spudich and Stein in this volume.

The proposed hypocenter for the 40 s event, together with its inferred slip distribution, were used in a forward modeling study of horizontal acceleration records at four sites. In a broader context, this example illustrates how information inferred at low frequencies, or in a limited frequency bandwidth, can be used as an aid in modeling data in higher frequency bands. The forward modeling makes use of the isochron formulation of radiated seismic energy from an extended fault to create synthetic acceleration envelopes. Although not discussed here, this technique can be merged with stochastic modeling methods to simulate ground acceleration in the near-source region of faults. For example, in Boore's method (1983), synthetic acceleration time histories are generated by windowing Gaussian white noise by a suitable envelope in the time domain; after which the signal is filtered in the frequency domain so as to exhibit the desired spectral characteristics of earthquake ground motion. Incorporating the isochron generated envelopes into this method affords the opportunity of modeling the high-frequency oscillations observed in ground motion time histories in a stochastic fashion, while generating the envelopes of these oscillations in a deterministic fashion from a given rupture scenario of an extended fault plane.

Acknowledgements

This research was carried out as part of the Irpinia Project, supported by ENEL S.p.A. under contract No. 1353. The authors wish to acknowledge Raniero Berardi and Carmine Petrungaro of ENEL for their important role in the execution and coordination of the various phases of this project. We would also like to acknowledge the following people for their generous support in various aspects of this study: Gianluca Valensise provided us with a subset of the original geodetic data collected by the Italian Military Geographic Institute; the modeling of high-frequency acceleration waveforms benefited from discussions with and en-

couragement from John Boatwright and Massimo Cocco; Paul Spudich provided us with his code for calculating travel times from extended fault planes to surface sites; and finally, Yomogida Okada provided us with his subroutines around which we constructed the code to calculate strain fields. Data processing and the production of figures were greatly facilitated by SAC, developed and distributed by LLNL.

REFERENCES

Amato, A. and G. Selvaggi (1993): Aftershock location and *P*-velocity structure in the epicentral region of the 1980 Irpinia earthquake, *Annali di Geofisica*, **36**, 3-15.

Arias, A. (1969): A measure of earthquake intensity, in *Seismic Design for Nuclear Power Plants*, edited by R. Hansen (Massachusetts Institute of Technology Press, Cambridge).

Berardi, R., A. Berenzi and F. Capozza (1981): Campania-Lucania earthquake on 23 November 1980: accelerometric recordings of the main quake and relating processes, in *Proceedings of the Progetto Finalizzato Geodinamica Meeting on «Sismicità dell'Italia: stato delle conoscenze scientifiche e qualità della normativa sismica»*, Udine, May 1981, 1-103.

Bernard, P. and R. Madariaga (1984): A new asymptotic method for the modeling of near field accelerograms, *Bull. Seismol. Soc. Am.*, **74**, 539-558.

Bernard, P. and A. Zollo (1989): The Irpinia (Italy) 1980 earthquake: detailed analysis of a complex normal faulting, *J. Geophys. Res.*, **94**, 1631-1647.

Bernard, P., A. Zollo, C. Trifu and A. Herrero (1993): Details of the rupture kinematics and mechanisms of the 1980 Irpinia earthquake: new results and remaining questions, *Annali di Geofisica*, **36**, 71-80.

Boore, D.M. (1983): Stochastic simulation of high-frequency ground motion based on seismological models of the radiated spectra, *Bull. Seismol. Soc. Am.*, **73**, 1865-1894.

Bracewell, R.N. (1978): *The Fourier Transform and its Applications* (McGraw-Hill electrical and electronic engineering series), 267-271.

Cocco, M. and F. Pacor (1993): Space-time evolution of the rupture process from the inversion of strong-motion waveforms, *Annali di Geofisica*, **36**, 109-130.

Cotecchia, V., A. Salvemini and N.A. Ventrella (1990): Interpretazione degli abbassamenti territoriali dal terremoto del 23 novembre 1980 e correlazioni con i danni osservati su talune strutture ingegneristiche dell'area epicentrale irpina, *Riv. Ital. Geotec.*, **24**, 145-158.

Dobry, R., I.M. Idriss and E. Ng (1978): Duration characteristics of horizontal components of strong-motion earthquake records, *Bull. Seismol. Soc. Am.*, **68**, 1487-1520.

Fregonese, R., A. Peano and M. Peronaci (1986): Synthetic modeling of low frequency strong motion data of Irpinia earthquake of 23 November 1980, in *Atti 2° Workshop su «Aree sismogenetiche e rischio sismico in Italia»*, Erice 26/8-4/9 1986, 131-150.

Giardini, D. (1993): Teleseismic observation of the November 23 1980, Irpinia earthquake, *Annali di Geofisica*, **36**, 17-25.

Harris, R. A. and P. Segall (1987): Detection of a locked zone at depth on the Parkfield, California, segment of the San Andreas fault, *J. Geophys. Res.*, **92**, 7945-7962.

Hartzell, S. (1989): Comparison of seismic waveform inversion results for the rupture history of a finite fault: application to the 1986 North Palm Springs, California, earthquake, *J. Geophys. Res.*, **94**, 7515-7534.

Hartzell, S. and T. Heaton (1983): Inversion of strong ground motion and teleseismic waveform data for the fault rupture history of the 1979 Imperial Valley, California, earthquake, *Bull. Seismol. Soc. Am.*, **73**, 1553-1583.

Hartzell, S. and M. Iida (1990): Source complexity of the 1987 Whittier Narrows, California, earthquake from the inversion of strong motion records, *J. Geophys. Res.*, **95**, 12475-12485.

Husid, R. (1969): Analisis de terremotos: analisis general, *Revista del IDIEM*, **8**, 21-42, Santiago, Chile.

Mendez, A.J. and J.E. Luco (1990): Steady state, near-source models of the Parkfield, Imperial Valley, and Mexicali Valley earthquakes, *J. Geophys. Res.*, **95**, 327-340.

Mendez, A.J., A.H. Olson and J.G. Anderson (1990): A norm minimization criterion for the inversion of earthquake ground motion, *Geophys. J. Int.*, **102**, 287-298.

Okada, Y. (1992): Internal deformation due to shear and tensile faults in a half-space, *Bull. Seismol. Soc. Am.*, **82**, 1018-1040.

Olson, A.H. and R.J. Apsel (1982): Finite faults and inverse theory with applications to the 1979 Imperial Valley earthquake, *Bull. Seismol. Soc. Am.*, **72**, 1969-2001.

Olson, A.H. and J.G. Anderson (1988): Implications of frequency domain inversion of earthquake ground motions for resolving the space-time dependence of slip on an extended fault, *Geophys. J. R. Astr. Soc.*, **94**, 443-455.

Pantosti, D. and G. Valensise (1990): Faulting mechanism and complexity of the 23 November, 1980 Campania-Lucania earthquake inferred from surface observations, *J. Geophys. Res.*, **95**, 15319-15341.

Pantosti, D. and G. Valensise (1993): Source geometry and long-term behavior of the 1980, Irpinia earthquake fault based on field geologic observations, *Annali di Geofisica*, **36**, 41-49.

Pingue, F., G. De Natale and P. Briole (1993): Modeling of the 1980 Irpinia earthquake source: constraints from geodetic data, *Annali di Geofisica*, **36**, 27-40.

Sirovich, L. and C. Chiaruttini (1993): The influence of source complexity on the polarization and azimuthal radiation of *S*-waves, and a simplified synthesis of the macroseismic field, *Annali di Geofisica*, **36**, 81-91.

Spudich, P.K.P. (1980): The DeHoop-Knopoff representation theorem as a linear inverse problem, *Geophys. Res. Lett.*, **9**, 717-720.

Spudich P. and L.N. Frazer (1984): Use of ray theory to calculate high-frequency radiation from earthquake

sources having spatially variable rupture velocity and stress drop, *Bull. Seismol. Soc. Am.*, **74**, 2061-2082.

TRIFUNAC, M.D. and A.G. BRADY (1975): A study of duration of strong earthquake ground motion, *Bull. Seismol. Soc. Am.*, **65**, 581-626.

TURCOTTE, D.L. and G. SCHUBERT (1982): *Geodynamics Applications of Continuum Physics to Geological Problems* (John Wiley & Sons), 348-380.

VACCARI, F., P. HARABAGLIA, P. SUHADOLC and G.F. PANZA (1993): The Irpinia (Italy) 1980 earthquake: waveform modeling of accelerometric data and macroseismic considerations, *Annali di Geofisica*, **36**, 93-107.

VALENSISE, G. (1993): Summary of contributions on the 23 November 1980, Irpinia earthquake, *Annali di Geofisica*, **36**, 345-351.

VALENSISE, G., A. AMATO, L. BERANZOLI, E. BOSCHI, M. COCCO, D. GIARDINI and D. PANTOSTI (1989): Un modello di sintesi del terremoto Campano-Lucano del 23 Novembre 1980, *Atti 8° Convegno G.N.G.T.S.*, Rome, 1989.

WESTAWAY, R. (1993): Fault rupture geometry for the 1980 Irpinia earthquake: a working hypothesis, *Annali di Geofisica*, **36**, 51-69.

WESTAWAY, R. and J. JACKSON (1987): The earthquake of 1980 November 23 in Campania-Basilicata (Southern Italy), *Geophys. J. R. Astr. Soc.*, **90**, 375-443.